

Origin and stability of generalized Wigner crystallinity in triangular moiré systems

Aman Kumar,^{1,2,*} Cyprian Lewandowski,^{1,2,†} and Hitesh J. Changlani^{1,2,‡}

¹*National High Magnetic Field Laboratory, Tallahassee, Florida 32310, USA*

²*Department of Physics, Florida State University, Tallahassee, Florida 32306, USA*

(Dated: September 24, 2024)

Generalized Wigner crystals (GWC) on triangular moiré superlattices, formed from stacking two layers of transition metal chalcogenides, have been recently observed at multiple fractional fillings of the moiré unit cell [Y. Xu et al., *Nature* 587, 214 - 218 (2020), X. Huang et al. *Nat. Phys.* 17, 715 - 719 (2021), H. Li et al., *Nature* 597, 650 - 654 (2021)]. Motivated by these experiments, tied with the need for an accurate microscopic description of these materials, we explore the theoretical origins of generalized Wigner crystallinity at $n = 1/3$ and $2/3$ filling. We demonstrate the limitations of theoretical descriptions of these moiré GWCs relying on truncated (finite-range) electron-electron interactions instead of a long-range Coulomb interaction. We validate our findings by studying both classical and quantum mechanical effects at zero and finite temperatures. More generally, we discuss the role of charge frustration in the theoretical extended Hubbard-model phase diagram, identifying a “pinball” phase, a partially quantum melted generalized Wigner crystal with coexisting solid and liquid-like features, with no classical analog. Quantum effects also explain the small, but experimentally detectable, asymmetry in the transition temperatures of the $n = 1/3$ and $2/3$ crystals. Our calculations reveal that the charge ordering temperature and the magnetic crossover temperature predicted using the long-range Coulomb interaction are correctly captured with appropriately renormalized nearest-neighbor interactions. The effective nearest-neighbor interaction strength is significantly weaker than previously reported, placing it close to a metal-insulator phase boundary. This observation has implications for future experiments that we discuss. We conclude by studying the dependence of melting temperatures on gate-to-sample separation and we also predict temperature scales at which magnetic crossovers should be observed.

Introduction – The study of moiré systems has opened up multiple new avenues of research in condensed matter physics [1–3]. Previously conjectured phases of electronic matter that were attributed to just the imagination of creative theorists are now being realized and observed in these platforms, e.g., Refs. [4–9]. The unique properties of moiré systems that allow for these proposed phases to be readily realized rely on the significant reduction in overall energy scales enabled by the moiré superlattice (while keeping strong correlations intact) combined with the tunability of carrier densities by the electrostatic gating characteristic of 2D materials. An excellent example of such theoretical and experimental synergy is shown by recent works that demonstrate how triangular lattice Hubbard model qualitatively explains the properties of moiré transition metal dichalcogenide systems (TMD) [6, 7, 10–16] that display itinerant ferromagnetism (above half filling) [17–19] and anti-ferromagnetism from kinetic frustration (below half filling) [20, 21], with observable effects at “intermediate” temperatures [19, 22, 23].

While the Hubbard model description of the moiré TMD systems has undoubtedly been very successful [24, 25], a crucial aspect missing is the role the long-range nature of the Coulomb interaction can play controlling the electronic phase diagram (e.g. see the discussion

on the importance of non-local/finite range interaction terms in Hubbard model in Ref. [26, 27]). In this work, we focus on the role of long-range Coulomb interaction in these systems and analyze the consequences of projecting it to a finite-range Hubbard model. Specifically, we systematically explore, at zero and finite temperature, both finite-range (FR) and long-range (LR) Hubbard models given by,

$$H = - \sum_{i < j, \sigma} t_{ij} c_{i, \sigma}^\dagger c_{j, \sigma} + \text{h.c.} + U \sum_i n_{i, \uparrow} n_{i, \downarrow} + \sum_{i < j} V_{ij} n_i n_j \quad (1)$$

where i, j refer to the sites of a (moiré) triangular lattice, σ is the spin index, and t_{ij} , U and V_{ij} refer to the hopping, on-site interaction strength and density-density interactions respectively, see Fig.1a. Here $n_{i, \sigma} \equiv c_{i, \sigma}^\dagger c_{i, \sigma}$ and $n_i \equiv n_{i, \uparrow} + n_{i, \downarrow}$ are the usual number operators. We focus specifically on the fillings (n) of $1/3$ and $2/3$ to make the physics of a long-range Coulomb interaction truncation the center of our discussion, leaving an exhaustive study of other fillings for future work.

The experimental platform that realizes the relevant physics for this manuscript is the moiré heterobilayer WSe_2/WS_2 system [6, 7, 10–12], which hosts generalized Wigner crystals (GWC) at fillings commensurate with the moiré superlattice enabled by the $\text{WSe}_2, \text{WS}_2$ lattice mismatch [14, 28]. Interest in GWCs has been fueled by recent experiments that used optical probes [6] and scanning tunneling microscopy (STM) [7] to confirm the presence of GWCs in moiré TMDs. In the STM work in particular, a state consistent with an expected $\sqrt{3} \times \sqrt{3}$ order was found in small local patches, however, vacancies in

* akumar@magnet.fsu.edu

† clewandowski@magnet.fsu.edu

‡ hchaglani@magnet.fsu.edu

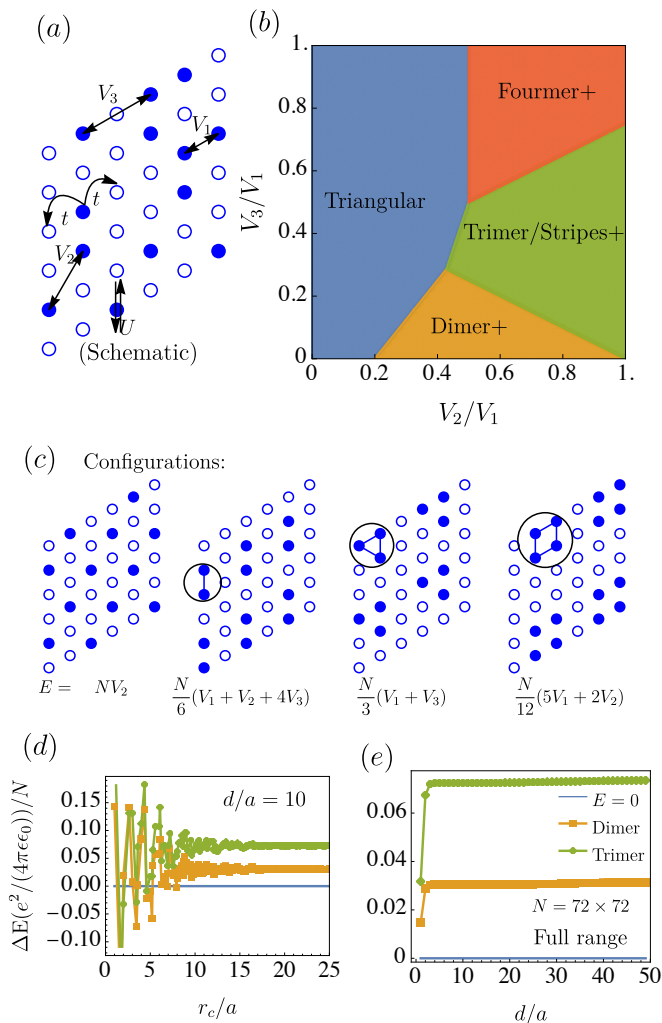


FIG. 1. (a) A schematic of $t - V$ model from Eq.(1). (b) Classical phase diagram of charge ground state configuration in the $V_1 - V_2 - V_3$ model. The + indicates the presence of degenerate configurations in addition to the one mentioned. (c) Real space configuration of triangular, dimer, trimer/stripes, fourmer, and their corresponding total energy. (d, e) The energy difference of the dimer and trimer configuration compared with triangular configuration as a function of interaction cutoff r_c/a and gate distance d/a , respectively. The computation is carried out on a 72×72 system.

the underlying charge order with motifs that visually resemble other orders are also seen. The nature of these insulating GWC orders has been studied theoretically through a mixture of theoretical techniques starting from continuum-model or Hubbard-model-like description and employing field theory, Hartree-Fock, DMFT, Monte-Carlo, density matrix renormalization group (DMRG), or exact diagonalization (ED) techniques[15, 29–37].

Our work addresses currently unresolved aspects of these experiments, contributing to the theoretical understanding of the moiré TMD systems and presenting both zero-temperature and finite-temperature studies in a unified framework. Our paper is structured in three parts,

each addressing one precise objective. The first objective is to demonstrate that while finite-range Hubbard models have the essential elements to describe a GWC, they are generally inadequate for a quantitative explanation of the experiments. This analysis involves a general exploration of the classical ($t = 0, U \rightarrow \infty$) and quantum mechanical phase diagram of Hamiltonian in Eq. (1) at zero temperature. The next objective is to understand the finite temperature melting of these GWCs. We build on the classical treatment that accurately modeled many aspects of the experiments [6], but did not address the role of quantum fluctuations - after all, it is not *a priori* clear if the melting of the GWC (at ~ 37 K) has any quantum origin given that the kinetic energy is $t \sim 20$ K. Our numerical calculations explain the small but experimentally detectable [6] (few Kelvin) difference in the transition temperatures of the $n = 1/3$ and $2/3$ GWC, that are exactly dual to one another at the classical level. A natural outcome of the first two objectives is the partial reconciliation of conflicting parameter sets chosen by different groups [6, 13, 38]. Our third objective is to predict the extent of the stability of GWC with screening gate distance (see also Ref. [15]) - a key component of the moiré TMD experimental setup. This objective aims to pave the way for informed experiment design by determining at what temperatures the magnetic correlations present in GWC [13, 16, 39–42], are most prominent and thus most easily detectable.

Classical phase diagram and competing charge states - To develop an intuition for the GWC problem, we first construct the classical charge ground state phase diagram ($t = 0$ and $U \rightarrow \infty$) for $n = 1/3$ of the Hamiltonian Eq. (1). This calculation serves as a helpful starting point for the analysis as the leading energy scale of the problem is the Coulomb interaction between electrons trapped in deep moiré potential wells[25] - a point to which we return later. We consider nearest (NN, strength $V_1 = 1$), next-nearest (NN, strength V_2) and next-to-next nearest neighbor interactions (NNN, strength V_3); our results are summarized in Fig. 1b,c. No double occupancy is allowed, i.e., $U = \infty$, and spin is irrelevant. The $n = 2/3$ results can be obtained by swapping the roles of particles and holes.

For small V_2, V_3 the $\sqrt{3} \times \sqrt{3}$ GWC is stable, as the total charge configuration completely avoids the V_1 and V_3 costs at the expense of a V_2 cost. However, other phases are favored for modest V_2/V_1 and V_3/V_1 . For example, for $V_3 = 0$, a value of $V_2/V_1 = 0.2$ stabilizes a “dimer” crystal, the state that arises out of a compromise - the system pays some V_1, V_2 and V_3 costs by pairing up into dimers, as shown in Fig. 1c. Interestingly, this periodic arrangement is degenerate with exponentially many (in system size) other exactly states including non-periodic configurations, suggesting a high amount of “charge frustration”. At larger V_3 , a crystal is formed out of a cluster of three charges, which we refer to as a “trimer”. This state pays no V_2 cost but pays some V_3 costs between trimers. It is degenerate with many other states, most

prominently a period-3 “stripe” state (periodic arrangement of one-dimensional lines of charges). In this state (which will feature in Fig. 2), all V_1 and V_3 costs are paid within each one-dimensional stripe. Then, when V_2 and V_3 are both large, a “fourmer” crystal, shown in Fig. 1c, is stabilized. In general, it is important to note that at low density, the system avoids energy penalties by clustering particles, even in the absence of any attractive interactions - reminiscent of a pairing mechanism discussed in Refs.[43] and recent reports of “bubble phases” in Landau levels [44].

We now ask where in the phase diagram of Fig. 1b are typical moiré TMD materials expected to be. To answer that question, it is necessary to compute the extended V_{ij} Hubbard parameters. Following Ref. [6], we consider a double-gate screened Coulomb interaction

$$V(\vec{r}) = \frac{e^2}{4\pi\epsilon\epsilon_0 a} \sum_{k=-\infty}^{k=\infty} \frac{(-1)^k}{\sqrt{\left(\frac{kd}{a}\right)^2 + \left(\frac{|\vec{r}|}{a}\right)^2}} \quad (2)$$

and calculate the relevant V_{ij} parameters. The above form of the Coulomb interaction assumes two gates symmetrically located (above and below) at a distance $d/2$ from the moiré system (as relevant for the experiment of Ref. [6]), however our conclusions should generalize, with appropriate quantitative modifications, to other gate configurations [7]. In the above calculation of V_{ij} parameters, we also assume that the Wannier functions are localized on a length scale much smaller than the moiré lattice constant (which is expected for this topologically trivial system that gives rise to the GWC [14, 28]). In such a case, it is reasonable to approximate the interactions as those between point charges, which we do for clarity. In principle, however, the Wannier function overlap can be incorporated (e.g. see Ref. [13, 14, 26]) into estimating the on-site Hubbard U and extended V_{ij} . While this treatment is expected to only provide a small correction to the extended V_{ij} parameters, it is essential for the estimation of the Hubbard U (e.g., as discussed in Ref. [38]). However, since our work focuses on fillings of significantly less than one electron per moiré cell, it is not necessary to compute U quantitatively - all that is important for our results is that U is large enough to prevent any appreciable double occupancy on a site.

As is explained in Appendix A, we treat the long-range nature of the interaction by tiling the finite size cluster (the fundamental unit cell) multiple times to cover all of space, and then use the arrangement to calculate the effective interaction between any two sites (including the site with itself) in the fundamental unit cell.

To highlight how the competition between ground states is sensitive to the range of truncation, we consider a sequence of models with increasing range r_c (the distance at which the interaction is truncated) i.e., increasing number of non-zero V_{ij} extended Hubbard model terms in Eq.1. Specifically, we take $V(\vec{r})$ to have the form in Eq. (2) for $r \equiv |\vec{r}| \leq r_c$ and $V(\vec{r}) = 0$ for

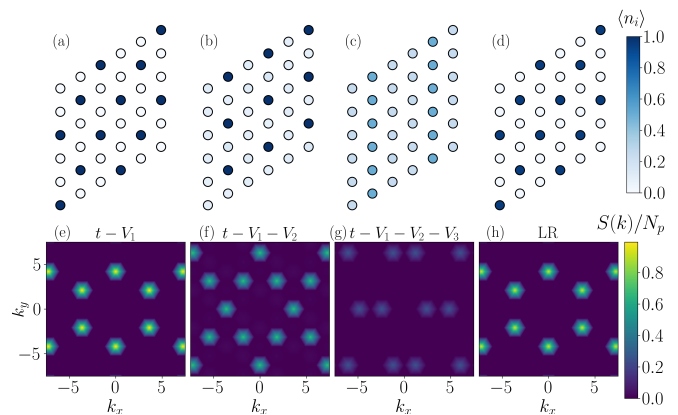


FIG. 2. Charge ground state configuration in real space (a-d) and momentum space (e-h) for finite-range and long-range models. The results are for different cutoffs r_c in the range of the interaction potential. We employ DMRG simulations with bond dimensions up to 10000.

$r > r_c$. In Fig. 1d, we plot, for $d/a = 10$, energy difference (per site) of each of the competing states we found in Fig. 1b as referenced with triangular energy. For NN interactions, indeed, the triangular $\sqrt{3} \times \sqrt{3}$ crystal is the ground state however, truncating to NNN yields the dimer crystal and truncating to higher neighbor interactions generically gives more complex ground states. Fig. 1e shows the competition between ground states for the (fully) long-range (LR) interaction (i.e., $r_c \rightarrow \infty$) as a function of d/a . When LR interaction is considered, we find that the $\sqrt{3} \times \sqrt{3}$ GWC is always the ground state for any gate distances $d/a \gtrsim 1$.

Quantum treatment, “pinball phase”, and state selection – The small energy differences between competing classical states, particularly when the interactions are long-ranged, as in Fig. 1d, highlight the need to account for quantum effects accurately. To do so, we consider the simplest possible kinetic term, the NN hopping, which was estimated to be much larger than other hoppings (see Table A.I). In principle, in analogy to the V_{ij} Hubbard terms in Eq.(1), the kinetic term could have contributions beyond NN hopping. However, since kinetic energy is significantly suppressed in GWCs and largely acts as a perturbation to ground states selected by the Coulomb interactions, we argue that it is sufficient to consider just the NN term to capture the relevant charge physics we discuss in this work. In future works, it would be interesting to study the role of extended hoppings, especially in parts of the phase diagram where multiple charge or magnetic orders compete closely [13, 38].

We obtain the quantum mechanical ground state on finite clusters using matrix product state (MPS) based DMRG calculations [45, 46]. On a given system size, DMRG is limited only by finite bond dimension, when this is inadequate DMRG favors low entanglement states such as those with broken translational symmetry. Given the 1-D nature of the MPS which is used to “snake

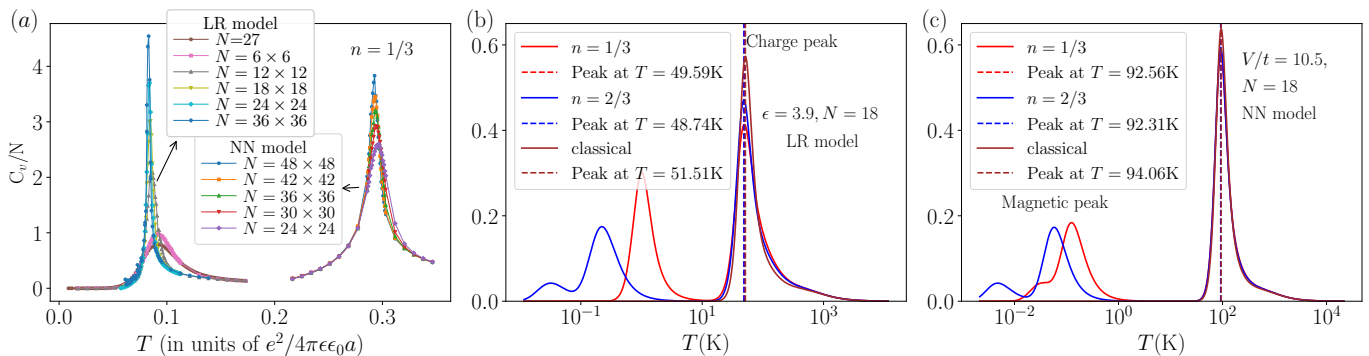


FIG. 3. Specific heat curves per particle (C_v/N). (a) C_v/N for the nearest neighbor finite-range and long-range models in classical limits. (b,c) C_v/N for a quantum calculation. We consider the effect of electron hopping for two different electron densities, $1/3$ and $2/3$, and show C_v/N for the long-range model and finite-range model, respectively.

through” a 2-D system, the accuracy of DMRG is typically limited on systems with periodic boundaries (torus in 2D) or those with long correlation lengths [47]. On the other hand, the torus geometry has the advantage of having no boundary effects and so is possibly more representative of the thermodynamic limit. Thus we interpret the results of our bond dimension-limited runs on tori, that favor symmetry-broken states with low entanglement, to be genuinely representative of the underlying physics, despite them not being exact eigenstates. To supplement these results and build confidence in our results, we have carried out additional DMRG calculations on cylinders. The quasi-1D nature of the cylinders, while conducive for DMRG, is known to affect the physics especially if the length of the cylinder is taken to be much larger than its width [48]. Given these caveats, we do arrive at similar qualitative conclusions on cylinders, see additional results and discussion in Appendix B.

The representative results for $n = 1/3$ for a sequence of FR and LR Hubbard models on a 6×6 torus (computed with a maximum bond dimension of 10000) are shown in Fig. 2a-d. All the finite-range models discussed in this section are obtained by taking the parameters from Ref. [6] (i.e. with $\epsilon = 3.9$ and $d/a = 10$, see also Table A.I in Appendix A) We plot the charge density ($\langle n_i \rangle$) on every lattice site and also show the Fourier transform of the density correlation function, Fig. 2e-h. In agreement with expectations, we find for the NN model with $V_1/t = 21.2$ that the $\sqrt{3} \times \sqrt{3}$ crystal is stable to quantum fluctuations, Fig. 2a. We also note that charge density is sharply localized on the sites of the $\sqrt{3} \times \sqrt{3}$ crystal, c.f. Fourier transform in Fig. 2e, confirming the identification of this charge density wave ground state with that of a GWC.

However, the ground state of the $V_1 - V_2$ model is strikingly distinct from the classical expectation - we find no evidence of stabilization of a dimer crystal or any of the other classically degenerate ground states. Instead, we see the appearance of charge centers (with $\langle n \rangle \approx 1$) at sites of a triangular crystal with a spacing of two (moiré) lattice constants, Fig. 2b,f. This emergent 2×2 triangu-

lar crystal accounts only for $1/4$ filling, and the remaining $1/3 - 1/4 = 1/12$ charge density was found to be delocalized on the other sites. This “partially melted” GWC arises out of a compromise - the system avoids paying both V_1 and V_2 costs between the charges on the “pinned” sites and also benefits from kinetic energy delocalization of the remaining charges. There is also a Coulomb energy cost associated with the delocalized charges interacting with the pinned charges, but overall, the first two effects dominate, leading to the stabilization of such a crystal. We envisage that while this $V_1 - V_2$ finite-range model does not govern the realistic moiré TMD system, the phase we have found here could be potentially realized in other platforms such as cold atoms [23, 49]. We also note that the phase we have found here shares many qualitative similarities with, but is distinct from, a “pinball liquid phase” [50] previously theoretically established at a different density $n = 1/2$ (quarter filling) and in an extended Hubbard model on the triangular lattice with only V_1 interactions.

The $V_1 - V_2 - V_3$ model for the parameter set in Table A.I yields a period-3 stripe ground state, resembling its classical counterpart - see Fig. 2c. Here, one of three equivalent directions of the triangular lattice is spontaneously selected. Unlike the classical result, however, charge localization is weakened in strength due to quantum fluctuations leading to smaller peaks in the Fourier transform of the charge density profile, Fig. 2h. It is interesting to observe that extended stripes are favored over local trimers - a possible mechanism is “order by disorder” which dictates how quantum state selection occurs among a collection of classically degenerate states [51, 52] and which has also been shown to be relevant for other materials with charge order [53].

Most importantly, we find that the LR model stabilizes a $\sqrt{3} \times \sqrt{3}$ GWC, see Fig. 2d. Resulting charge density localization is identical to the V_1 only model, with only minor quantitative differences in the densities on the GWC sites, c.f. Fig. 2e,h. This result suggests that the NN model, with appropriate renormalization of the extended interaction V_1 , may capture the essential physics

of GWC melting at finite temperature, which we will explore next.

Finite temperature properties of GWC – We now proceed to analyze the finite temperature properties of the GWCs. We begin by considering the classical model ($t \rightarrow 0$, $U \rightarrow \infty$ in Eq.(1)). Fig. 3a shows the specific heat per site C_v/N of the LR and truncated NN classical models for the case of $d/a = 10$, computed with classical Monte Carlo. We find that despite having the same classical ground state, the T_c of the LR model is a factor of ≈ 3.6 smaller than that of the NN model, indicating that the long-range tail significantly renormalizes the NN interaction.

With a classical expectation of the melting behavior in place, we now consider a quantum mechanical finite-temperature study of the Hamiltonian in Eq. 1. While some quantitative differences are to be expected due to finite size effects, the location of T_c for system sizes as small as $N = 27$ sites is broadly consistent with much larger sizes (to within 10%). Given that meaningful conclusions and trends can be drawn from small clusters, we compute the quantum mechanical specific heat for the $N = 18$ system (see Appendix C for cluster shape and symmetries used). For consistency, we also consider (using the same numerical procedure) the “classical” case with $t = 0$ but with otherwise identical parameters, i.e., U large but finite. Our results are shown in Fig. 3b,c on a log temperature scale for the LR and NN models, respectively. The NN interaction strength is in the ballpark of that studied in Ref. [38] where ϵ was chosen to be 10, but the model was truncated to NN interactions.

The differences in the choices of ϵ (see for example work of Ref. [6] and Ref. [38]) followed by truncation (or lack of it) can potentially reconcile parameter sets that otherwise look very different. In particular, two effects compete with one another: increasing ϵ has the effect of decreasing the overall strength of Coulomb interactions and hence lowering the ordering temperature, and truncating the LR interaction eliminates the overall reduction that comes from the long-range tail, in turn increasing the ordering temperature. The end result is that the effective V_1/t used in the NN model is approximately 10.5 [38]. We find that this, in turn, results in the GWC temperature melting temperature that is a factor of roughly two higher (see Fig. 3c) than that measured in experiment and reproduced by classical Monte Carlo with the full LR model with $\epsilon = 3.9$ [6].

The quantum-mechanical finite-temperature simulations shows that the entropy is released in two steps for both LR and NN models. The low-temperature bump (crossover) corresponds to the destruction of finite-range magnetic correlations (there is no true long order at finite temperature due to the Mermin-Wagner theorem [54]). As magnetic correlations are quantum mechanical in nature, they are completely absent in the classical calculations. The higher temperature peak corresponds to the melting of the charge order. The suppression of kinetic energy in the GWC means that its melting is essentially

classical origin, this is particularly true for the NN model with $V_1/t = 10.5$, which shows no detectable difference in the location of T_c for $n = 1/3$ and $2/3$ and the classical model. The LR model however, with effectively weaker interactions, shows lower T_c s compared to the classical case. We attribute this to the small amount of quantum melting of the ground states. Additionally, the kinetic energy term on the triangular lattice breaks the particle-hole symmetry of the classical model; this manifests itself as the (roughly) 1 K difference between T_c of $n = 1/3$ and $2/3$ cases, which is in the ballpark of the experimental findings [6].

The difference between $n = 1/3$ and $2/3$ manifests itself even more prominently in the low-temperature magnetic features, which remain to be experimentally explored, c.f. Fig.3b. Our calculations predict the magnetic crossover temperatures in the range 0.2 K - 1 K, with the particle-hole differences on the scale of few hundred mK). These magnetic crossover scales are within experimentally realizable range, suggesting that future experiments sensitive to spin texture (e.g., NV center scanning techniques, spin-polarized scanning tunneling microscopy or nanoSQUID) could resolve the nature of the various spin ground states[13, 16, 39–42].

Predictions for quantum and thermal melting of GWC – We now study the possible quantum mechanical “melting” of the GWC charge order by controlling the screening environment by tuning d/a . Smaller d corresponds to a stronger screening manifesting in a shorter length scale over which the LR Coulomb interaction becomes suppressed by the gate. This suppression of effective LR Coulomb interaction range with decreasing d/a should eventually drive the system to metallicity despite U being large because of the low density of particles or holes. This is quantitatively established in Fig. 4a, which shows the value of the order parameter computed on the $N = 27$ site cluster (see Appendix C) from ED using the Lanczos method for both $n = 1/3$ and $2/3$. (The order parameter corresponds to the Fourier component of the density-density correlation function at the K points.) At large d/a , its value is approximately constant (with a small decrease compared to the analytical expectation due to the finite size effect). In contrast, on lowering d/a , its value rapidly decreases for $d/a \lesssim 1$. We note in passing that given that $a \approx 8$ nm, the $d/a \lesssim 1$ is within experimental range of the hBN dielectric thicknesses [55, 56].

The dependence of the screened Coulomb interaction from Eq.(2) as a function of d/a does not immediately reveal why the order parameter should be essentially constant for large d/a . For example, V_1 grows (albeit slowly) with d/a , see Fig.4b (red, $V_{1,\text{Coulomb}}$ curve), and tail decays rapidly with d/a , see. Fig. A.1. We propose that the origin of the relative independence of the order parameter with d/a stems from the “cancellations” of the long-range tail which yield an effective NN strength. This NN strength is much smaller than the V_1 computed from the Coulomb interaction alone, confirming the expectation we had from the classical specific heat analysis.

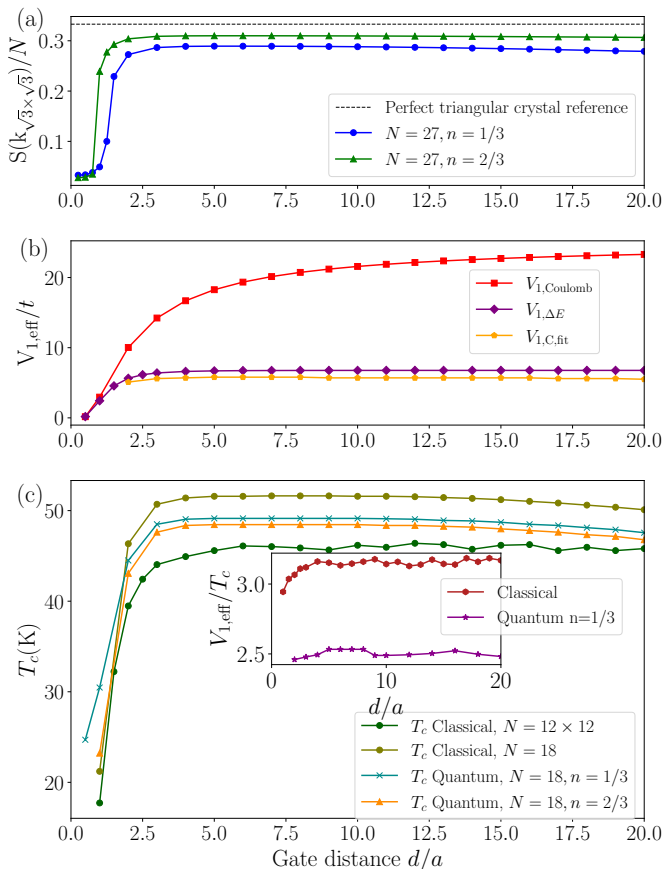


FIG. 4. (a) charge structure factor at a representative momentum point of the $\sqrt{3} \times \sqrt{3}$ order peaks as a function of d/a . We employed the Lanczos method with 400 Krylov vectors. The dotted line represents the expected value for a perfect $\sqrt{3} \times \sqrt{3}$ order. (b) The effective NN $V_{1,\text{eff}}/t$ interaction as a function of d/a obtained from: the interaction potential ($V_{1,\text{Coulomb}}$, Eq. (2), [6]), one defect energy ($V_{1,\Delta E}$), and from fitting the specific heat curve of the long-range and finite-range nearest neighbor models ($V_{1,\text{C,fit}}$). (c) The critical temperature T_c corresponds to charge melting for three cases: classical, $n = 1/3$, and $n = 2/3$ as a function of d/a . (inset) Ratio of the $V_{1,\text{eff}}$ to T_c using $V_{1,\Delta E}$ (classical) and $V_{1,\text{C,fit}}$ (quantum) from (b).

We verify this hypothesis in two complementary ways, as shown in Fig 4b. First, at the purely classical level in an LR model, we calculate the energy to create a “defect” (by moving one charge in the GWC to a neighboring unoccupied site of the triangular lattice). This energy corresponds to $2V_{1,\Delta E}$ (see Appendix E), the energy it would cost in the NN model. This $V_{1,\Delta E}/t$ is found to be roughly 6.9 and is essentially independent of d/a (purple curve in Fig 4b). In the second method, we vary the V_1 NN interaction (we refer to the value of this V_1 as $V_{1,\text{C,fit}}$) such that its specific heat profile most closely matches that of the LR quantum model. For this purpose, we define a cost function (see Appendix E), and we find that this procedure well reproduces both the magnetic bump and charge peak. We find that this value is in the same

ballpark $V_{1,\text{C,fit}}/t \approx 5.7$, and importantly it is essentially again independent of d/a confirming our hypothesis (orange curve in Fig 4b). We note that both these values of $V_{1,\text{eff}}/t$ (estimated using the two different methods) are only slightly above the ballpark of the metal-insulator transition (MIT) for $n = 1/3$ ($V_{\text{MIT}}/t \approx 4$ [57]), but significantly less than what has been reported for these moiré materials (e.g. Refs. [38]). The transition is also expected to be a first order one [58]. This closeness to a phase boundary suggests that local disorder may stabilize pockets of insulating (charge-ordered) and metallic regions. We conjecture that this proximity to the MIT transition perhaps lies at the origins of the real-space signal variation of what should be a pristine $\sqrt{3} \times \sqrt{3}$ GWC in the STM maps of Ref. [7].

Lastly, we comment that the impact of this effective NN renormalization is also confirmed by plotting the T_c of the classical and quantum models as a function of d/a in Fig. 4c. As expected, T_c follows $V_{1,\text{eff}}$ rather than V_1 which we also check by plotting the ratio of $V_{1,\text{eff}}/T_c$ in the inset. Similar observation was noted for select values of d/a in Ref. [6] in the classical calculation, but was not explained. Surprisingly, the temperature of the magnetic bump scales is inversely proportional to $(V_{1,\text{eff}})^3$ in agreement with a simplest exchange process in fourth-order perturbation theory (See Appendix F for more details).

Outlook and Summary In summary, we have studied zero- and finite-temperature properties of a generalized Wigner crystal at $n = 1/3$ and $n = 2/3$ filling. We employed a mixture of numerical techniques to describe an effective extended Hubbard model on the triangular lattice, relevant to moiré materials. Crucially, throughout the manuscript, we related the extended Hubbard model parameters to realistic values expected from the Coulomb interaction and tight-binding estimates of the band structure.

On the theoretical front, our results introduce systematic complementary procedures for mapping a long-range Coulomb model to a NN Hubbard model. Our method for matching the specific heat is in the spirit of matching partition functions (or other density matrices of excited states) that has previously been employed in the context of single layer graphene [59–61]. We showed that when the GWC physics is (largely) controlled by classical effects (i.e., Coulomb interaction dominates; classical and quantum charge order temperature are nearly identical) then the total quantum mechanical LR model can be (approximately) mapped to an NN model by considering the energy of creating a single charge “defect”. This renormalization should be strongly dependent on the underlying charge-ordered GWC itself and it will be interesting to see how this impacts the physics of fillings beyond what has been considered here. We also caution that while our renormalization procedure correctly matches the NN and LR charge ordering and magnetic crossover temperatures, this does not necessarily imply that the two models are equivalent in all their aspects; for example, they may differ in the many-body excitation

gap [62, 63]. Understanding the limitations of such effective mappings is something we intend to investigate in future work. More generally, however, we anticipate that this procedure may help in future theoretical studies of the GWC (and moiré systems) in general. Through this mapping, we realized that the GWC systems are much closer to the metal-insulator transition than the previous estimates of the NN interaction, based on truncating the LR interaction, would predict. Our results clarify that although truncation of the LR interaction can stabilize a plethora of charge-ordered states, it must be treated with caution - a sentiment shared with many frustrated magnetic systems where long-range tails have been found to be important not only quantitatively but also qualitatively (see for e.g. work in the context of classical spin ice [64–66]).

Finally, our results explain several outstanding experimental puzzles. First, we showed that despite the kinetic energy being comparable to charge ordering transition T_c , its role is significantly suppressed. However, we demonstrated how the role of kinetic energy is still important for quantitatively capturing the small asymmetry in the experimentally detected T_c at $n = 1/3$ and

$n = 2/3$ [6]. Next, by mapping the LR model to an effective NN model that correctly captures the T_c , we showed that the GWC is near the MIT, possibly explaining the motifs seen in the STM imaging of Ref. [7]. Lastly, we demonstrated how experiments can control the charge ordering to magnetic ordering temperature by adjusting the gate-to-sample distance. This tuning knob we propose can be used to probe the precise microscopic spin nature of the GWC experimentally.

Acknowledgements – We thank V. Dobrosavljevic and V. Elser for useful discussions and for pointing us to the relevant literature, and results, and O. Tchernyshyov and S. Sherif for insights from complementary work. The DMRG simulations were performed using the TeNPy library. We acknowledge support from the National High Magnetic Field Laboratory (NHMFL). The NHMFL is supported by the National Science Foundation through NSF/DMR-2128556 and the state of Florida. A.K. was supported through a Dirac postdoctoral fellowship at National High Magnetic Field Laboratory. C.L. is supported by start-up funds from Florida State University and the National High Magnetic Field Laboratory. H.J.C acknowledges funding from National Science Foundation Grant No. DMR 2046570.

-
- [1] E. Y. Andrei, D. K. Efetov, P. Jarillo-Herrero, A. H. MacDonald, K. F. Mak, T. Senthil, E. Tutuc, A. Yazdani, and A. F. Young, *Nature Reviews Materials* **6**, 201–206 (2021).
- [2] K. F. Mak and J. Shan, *Nature Nanotechnology* **17**, 686–695 (2022).
- [3] L. Balents, C. R. Dean, D. K. Efetov, and A. F. Young, *Nature Physics* **16**, 725–733 (2020).
- [4] Y. Cao, V. Fatemi, S. Fang, K. Watanabe, T. Taniguchi, E. Kaxiras, and P. Jarillo-Herrero, *Nature* **556**, 43 (2018).
- [5] Y. Tang, L. Li, T. Li, Y. Xu, S. Liu, K. Barmak, K. Watanabe, T. Taniguchi, A. H. MacDonald, J. Shan, and K. F. Mak, *Nature* **579**, 353 (2020).
- [6] Y. Xu, S. Liu, D. A. Rhodes, K. Watanabe, T. Taniguchi, J. Hone, V. Elser, K. F. Mak, and J. Shan, *Nature* **587**, 214–218 (2020).
- [7] H. Li, S. Li, E. C. Regan, D. Wang, W. Zhao, S. Kahn, K. Yumigeta, M. Blei, T. Taniguchi, K. Watanabe, *et al.*, *Nature* **597**, 650 (2021).
- [8] K. Kang, B. Shen, Y. Qiu, Y. Zeng, Z. Xia, K. Watanabe, T. Taniguchi, J. Shan, and K. F. Mak, *Nature* **628**, 522–526 (2024).
- [9] H. Park, J. Cai, E. Anderson, Y. Zhang, J. Zhu, X. Liu, C. Wang, W. Holtzmann, C. Hu, Z. Liu, T. Taniguchi, K. Watanabe, J.-H. Chu, T. Cao, L. Fu, W. Yao, C.-Z. Chang, D. Cobden, D. Xiao, and X. Xu, *Nature* **622**, 74–79 (2023).
- [10] C. Jin, Z. Tao, T. Li, Y. Xu, Y. Tang, J. Zhu, S. Liu, K. Watanabe, T. Taniguchi, J. C. Hone, L. Fu, J. Shan, and K. F. Mak, *Nature Materials* **20**, 940–944 (2021).
- [11] E. C. Regan, D. Wang, C. Jin, M. I. Bakti Utama, B. Gao, X. Wei, S. Zhao, W. Zhao, Z. Zhang, K. Yumigeta, M. Blei, J. D. Carlström, K. Watanabe, T. Taniguchi, S. Tongay, M. Crommie, A. Zettl, and F. Wang, *Nature* **579**, 359–363 (2020).
- [12] X. Huang, T. Wang, S. Miao, C. Wang, Z. Li, Z. Lian, T. Taniguchi, K. Watanabe, S. Okamoto, D. Xiao, S.-F. Shi, and Y.-T. Cui, *Nature Physics* **17**, 715–719 (2021).
- [13] H. Pan, F. Wu, and S. Das Sarma, *Physical Review B* **102**, 201104 (2020).
- [14] F. Wu, T. Lovorn, E. Tutuc, and A. H. MacDonald, *Phys. Rev. Lett.* **121**, 026402 (2018).
- [15] N. Morales-Durán, P. Potasz, and A. H. MacDonald, *Phys. Rev. B* **107**, 235131 (2023).
- [16] S. F. Ung, J. Lee, and D. R. Reichman, *Phys. Rev. B* **108**, 245113 (2023).
- [17] B. S. Shastry, H. R. Krishnamurthy, and P. W. Anderson, *Phys. Rev. B* **41**, 2375 (1990).
- [18] M. Davydova, Y. Zhang, and L. Fu, *Phys. Rev. B* **107**, 224420 (2023).
- [19] K. Lee, P. Sharma, O. Vafek, and H. J. Changlani, *Physical Review B* **107**, 235105 (2023).
- [20] J. O. Haerter and B. S. Shastry, *Phys. Rev. Lett.* **95**, 087202 (2005).
- [21] J. O. Haerter, M. R. Peterson, and B. S. Shastry, *Phys. Rev. Lett.* **97**, 226402 (2006).
- [22] I. Morera, M. Kanász-Nagy, T. Smolenski, L. Ciorciaro, A. Imamoglu, and E. Demler, *Physical Review Research* **5**, L022048 (2023).
- [23] M. Xu, L. Haldar Kendrick, A. Kale, Y. Gang, G. Ji, R. T. Scalettar, M. Lebrat, and M. Greiner, *arXiv e-prints*, arXiv:2212.13983 (2022), arXiv:2212.13983 [cond-mat.quant-gas].
- [24] Y. Tang, L. Li, T. Li, Y. Xu, S. Liu, K. Barmak, K. Watanabe, T. Taniguchi, A. H. MacDonald, J. Shan,

- and K. F. Mak, *Nature* **579**, 353–358 (2020).
- [25] F. Wu, T. Lovorn, E. Tutuc, and A. H. MacDonald, *Phys. Rev. Lett.* **121**, 026402 (2018).
- [26] N. Morales-Durán, N. C. Hu, P. Potasz, and A. H. MacDonald, *Phys. Rev. Lett.* **128**, 217202 (2022).
- [27] Y. Tan, P. K. H. Tsang, V. Dobrosavljević, and L. Rademaker, *Phys. Rev. Res.* **5**, 043190 (2023).
- [28] Y. Zhang, N. F. Q. Yuan, and L. Fu, *Phys. Rev. B* **102**, 201115 (2020).
- [29] Y. Tan, P. K. H. Tsang, V. Dobrosavljević, and L. Rademaker, *Phys. Rev. Res.* **5**, 043190 (2023).
- [30] S. Musser, T. Senthil, and D. Chowdhury, *Phys. Rev. B* **106**, 155145 (2022).
- [31] Y. Zhang, T. Liu, and L. Fu, *Phys. Rev. B* **103**, 155142 (2021).
- [32] Y. Yang, M. A. Morales, and S. Zhang, *Phys. Rev. Lett.* **132**, 076503 (2024).
- [33] B. Padhi, R. Chitra, and P. W. Phillips, *Phys. Rev. B* **103**, 125146 (2021).
- [34] M. Matty and E.-A. Kim, *Nature Communications* **13**, 10.1038/s41467-022-34683-x (2022).
- [35] N. Morales-Durán, A. H. MacDonald, and P. Potasz, *Phys. Rev. B* **103**, L241110 (2021).
- [36] B. Padhi, R. Chitra, and P. W. Phillips, *Phys. Rev. B* **103**, 125146 (2021).
- [37] A. Biborski and M. Zegrodnik, *arXiv preprint arXiv:2409.11202* (2024).
- [38] J. Motruk, D. Rossi, D. A. Abanin, and L. Rademaker, *Phys. Rev. Res.* **5**, L022049 (2023).
- [39] N. C. Hu and A. H. MacDonald, *Phys. Rev. B* **104**, 214403 (2021).
- [40] H. Pan and S. Das Sarma, *Phys. Rev. Lett.* **127**, 096802 (2021).
- [41] H. Pan and S. Das Sarma, *Phys. Rev. B* **105**, 041109 (2022).
- [42] N. Kaushal, N. Morales-Durán, A. H. MacDonald, and E. Dagotto, *Communications Physics* **5**, 10.1038/s42005-022-01065-0 (2022).
- [43] V. Crépel and L. Fu, *Science Advances* **7**, 10.1126/sciadv.abh2233 (2021).
- [44] F. Yang, R. Bai, A. A. Zibrov, S. Joy, T. Taniguchi, K. Watanabe, B. Skinner, M. O. Goerbig, and A. F. Young, *Phys. Rev. Lett.* **131**, 226501 (2023).
- [45] S. R. White, *Phys. Rev. Lett.* **69**, 2863 (1992).
- [46] J. Hauschild and F. Pollmann, *SciPost Phys. Lect. Notes*, **5** (2018), code available from <https://github.com/tenpy/tenpy>, *arXiv:1805.00055*.
- [47] E. Stoudenmire and S. R. White, *Annual Review of Condensed Matter Physics* **3**, 111 (2012).
- [48] A. W. Sandvik, *Phys. Rev. B* **85**, 134407 (2012).
- [49] N. R. Cooper, J. Dalibard, and I. B. Spielman, *Rev. Mod. Phys.* **91**, 015005 (2019).
- [50] J. Merino, A. Ralko, and S. Fratini, *Phys. Rev. Lett.* **111**, 126403 (2013).
- [51] J. Villain, R. Bidaux, J.-P. Carton, and R. Conte, *Journal de Physique* **41**, 1263 (1980).
- [52] C. L. Henley, *Phys. Rev. Lett.* **62**, 2056 (1989).
- [53] D. Subires, A. Korshunov, A. H. Said, L. Sánchez, B. R. Ortiz, S. D. Wilson, A. Bosak, and S. Blanco-Canosa, *Nature Communications* **14**, 1015 (2023).
- [54] N. D. Mermin and H. Wagner, *Phys. Rev. Lett.* **17**, 1133 (1966).
- [55] P. Stepanov, I. Das, X. Lu, A. Fahimniya, K. Watanabe, T. Taniguchi, F. H. L. Koppens, J. Lischner, L. Levitov, and D. K. Efetov, *Nature* **583**, 375–378 (2020).
- [56] Y. Saito, J. Ge, K. Watanabe, T. Taniguchi, and A. F. Young, *Nature Physics* **16**, 926–930 (2020).
- [57] Y. Zhou, D. Sheng, and E.-A. Kim, *arXiv preprint arXiv:2312.03828* (2023).
- [58] A. Camjayi, K. Haule, V. Dobrosavljević, and G. Kotliar, *Nature Physics* **4**, 932–935 (2008).
- [59] M. Schüler, M. Rösner, T. O. Wehling, A. I. Lichtenstein, and M. I. Katsnelson, *Phys. Rev. Lett.* **111**, 036601 (2013).
- [60] H. J. Changlani, H. Zheng, and L. K. Wagner, *The Journal of Chemical Physics* **143**, 102814 (2015), <https://pubs.aip.org/aip/jcp/article-pdf/doi/10.1063/1.4927664/15502754/102814.1.online.pdf>.
- [61] H. Zheng, H. J. Changlani, K. T. Williams, B. Busemeyer, and L. K. Wagner, *Frontiers in Physics* **6**, 10.3389/fphy.2018.00043 (2018).
- [62] S. Mahmoodian, L. Rademaker, A. Ralko, S. Fratini, and V. Dobrosavljević, *Phys. Rev. Lett.* **115**, 025701 (2015).
- [63] Y. Pramudya, H. Terletska, S. Pankov, E. Manousakis, and V. Dobrosavljević, *Phys. Rev. B* **84**, 125120 (2011).
- [64] A. P. Ramirez, A. Hayashi, R. J. Cava, R. Siddharthan, and B. S. Shastry, *Nature* **399**, 333 (1999).
- [65] R. G. Melko and M. J. P. Gingras, *Journal of Physics: Condensed Matter* **16**, R1277 (2004).
- [66] N. Anand, K. Barry, J. N. Neu, D. E. Graf, Q. Huang, H. Zhou, T. Siegrist, H. J. Changlani, and C. Beekman, *Nature Communications* **13**, 3818 (2022).
- [67] S. W. de Leeuw, J. W. Perram, and E. R. Smith, *Proceedings of the Royal Society of London Series A* **373**, 27 (1980).

Appendix A: Interaction potential, Hamiltonian parameters and adaptation to finite systems

For two metallic gates placed symmetrically at distance $d/2$ above and below the TMD moiré bilayer, the effective classical potential between two point charges can be computed with the method of image charges. The result is,

$$V(\vec{r}) = \frac{e^2}{4\pi\epsilon\epsilon_0 a} \sum_{k=-\infty}^{k=\infty} \frac{(-1)^k}{\sqrt{\left(\frac{kd}{a}\right)^2 + \left(\frac{|\vec{r}|}{a}\right)^2}} \quad (\text{A.1})$$

where a is the moiré lattice constant, ϵ_0 is the permittivity (dielectric constant) of free space and ϵ is dimensionless. Note that we work directly with this expression for point charges on the triangular lattice - it is implicitly assumed that the extent of the Wannier function, centered on every moiré triangular lattice site, is much smaller than the distance between the two moiré sites. (See also the discussion in the main text).

In Fig. A.1a we plot $V(r)$ in units of $\frac{e^2}{4\pi\epsilon\epsilon_0 a}$ for various representative values of d/a . As expected, for larger d/a the potential is less screened (induced charges on the gates have less effect on the interaction between charges) while for smaller d/a the screening is stronger. This is evidenced by a more rapid decay with r/a for smaller d/a . In Fig. A.1b we also compare the numerically computed

$V(r)$, for $d/a = 10$, with the analytic form for large r/a that confirms the exponential decay of the potential.

Additionally, the overall magnitude of $V_1 \equiv V(r = a)$ increases with increasing d/a . In the large d/a limit we are able to approximate the series in Eq. (A.1) by the compact expression,

$$V_1 = \frac{e^2}{4\pi\epsilon\epsilon_0 a} \left(1 - \frac{2 \ln 2}{d/a}\right). \quad (\text{A.2})$$

Both the numerically computed V_1 and the approximate form are plotted in Fig. A.1c.

In Table A.I we have also tabulated the parameter sets (both with truncated/finite-range and long-range interactions) that appeared in the main text. The value of the NN hopping was taken from Ref. [38].

All our calculations were carried out on finite size systems (which can be thought of as the fundamental unit cell), where one must systematically account for truly long-range interactions to make meaningful statements about the thermodynamic limit. Conceptually, one must imagine all of space to be tiled by translating the finite unit cell along two lattice vectors. Each charge in the fundamental unit cell then sees another charge in the same cell and its “images” (not to be confused with the image charges used to derive the screened potential) in the other tiled unit cells. Thus the Hamiltonian on finite systems is given by,

$$H = - \sum_{i < j, \sigma} t_{ij} c_{i,\sigma}^\dagger c_{j,\sigma} + \text{h.c.} + U \sum_i n_{i,\uparrow} n_{i,\downarrow} + \sum_{i < j} \tilde{V}_{ij} n_i n_j + \sum_i \tilde{V}_{ii} n_i n_i \quad (\text{A.3})$$

where \tilde{V}_{ij} and \tilde{V}_{ii} are effective interaction potentials that account for the intra and inter-unit cell contributions.

$$\tilde{V}_{ij} = \sum_{n_1, n_2 = -\infty}^{\infty} V(\vec{r}_{ij} + n_1 \vec{L}_1 + n_2 \vec{L}_2) \quad (\text{A.4})$$

$$\tilde{V}_{ii} = \sum_{\substack{n_1, n_2 = -\infty \\ (n_1, n_2) \neq (0,0)}}^{\infty} V(n_1 \vec{L}_1 + n_2 \vec{L}_2) \quad (\text{A.5})$$

where \vec{L}_1 and \vec{L}_2 are inter unit cell translation vectors. In practice, these sums cannot be carried out exactly, and must be approximated (to very high accuracy) by truncating the limits on n_1 and n_2 to $\pm N_{max}$. For all d/a considered here, we find that it is sufficient to set $N_{max} = 100$ in each direction. The rapid convergence with this parameter is a direct result of the exponential decay - it is known that when the interactions are not screened, methods such as Ewald summation must be applied to get the effective potential [65–67].

Appendix B: DMRG results on cylinders

In the main text we discussed results based on ground state DMRG calculations carried on the 6×6 torus geom-

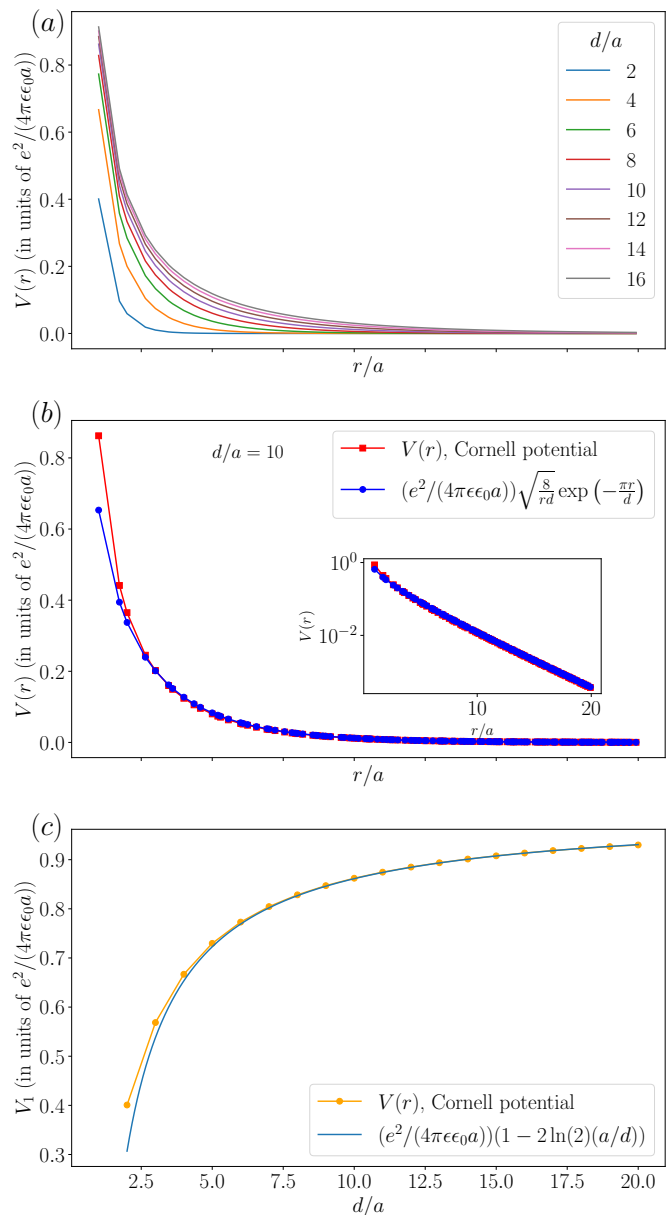


FIG. A.1. (a) Interaction potential $V(r)$ vs r/a for various representative values of d/a . (b) $V(r)$ vs r/a for the specific case of $d/a = 10$ showing comparison with the analytic asymptotic form (for large r/a). The inset shows the excellent matching of curves on a log scale. (c) $V_1 \equiv V(r = a)$ as a function of d/a . The asymptotic expression for large d/a is also plotted.

SN	Parameter values		
	t (meV)	U (meV)	V_{ij} (meV)
1	1.81	$75 t$	$V_1 = 10.5 t$, Ref [38]
2	1.81	$75 t$	$V_1 = 39.92$, $V_2 = 20.44$, $V_3 = 16.89$
3	1.81	$75 t$	$a = 8$ nm, $\epsilon = 3.9$, $d/a = 10$
4	0	∞	$a = 8$ nm, $\epsilon = 3.9$, $d/a = 10$

TABLE A.I. Summary of parameter sets used in the literature. All energy units are in meV. The functional form of the long range model is discussed in the text.

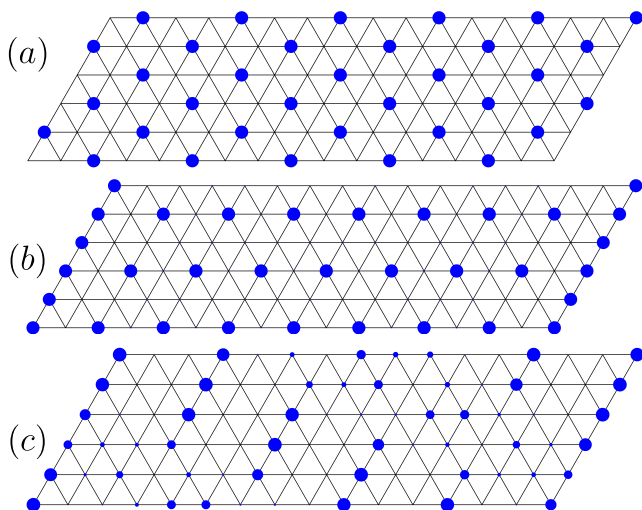


FIG. A.2. Ground state local charge density $\langle n_i \rangle$ from DMRG on every site i for three models (obtained from the long-range model) with truncated interactions up to (a) first neighbor, (b) second neighbor and (c) third neighbor. The sizes of the blue circles are proportionate to $\langle n_i \rangle$. The DMRG simulations are employed with bond dimension up to 8000 and energy convergence ΔE is $O(10^{-7})$.

etry. Since the kinetic energy (quantum) term is small compared to the Coulomb energy, and there are many competing classical configurations, some dependence on the finite system shape and size is expected. This could be potentially magnified in the vicinity of critical points in the phase diagram.

To build confidence in our results obtained for the torus, we have carried out additional DMRG calculations on cylindrical geometries of width 6. In Fig. A.2 we show results for the local charge density $\langle n_i \rangle$ (on every site i) computed in the ground state of three finite-range models that were obtained by truncating the full LR model to NN (Fig. A.2a), NNN (Fig. A.2b) and NNNN neighbor interactions (Fig. A.2c). In all three cases the hopping is taken to be NN. (For the list of parameters used, refer to Table A.I.) The diameter of the blue circles in the figure is proportionate to $\langle n_i \rangle$.

For the $t - V_1$ model (in Fig. A.2a) we see a clear $\sqrt{3} \times \sqrt{3}$ triangular crystal. The blue circles correspond to a charge density close to (but less than) 1, suggesting some melting of the classical Wigner crystalline order due to quantum fluctuations. For the $t - V_1 - V_2$ model (in Fig. A.2b) we observe a 2×2 Wigner crystal in the bulk, but to do so we had to minimize boundary effects by adjusting the overall charge density. Specifically, we simulated charge densities in the vicinity of (and slightly higher than) $1/3$, the charges in excess of the $1/3$ density migrated to the open boundary edge - this is the system's mechanism for minimizing the Coulomb cost. The bulk of the cylinder was left with an average density of $1/3$, which we take to be representative of the thermodynamic limit. We have also shown only the result from

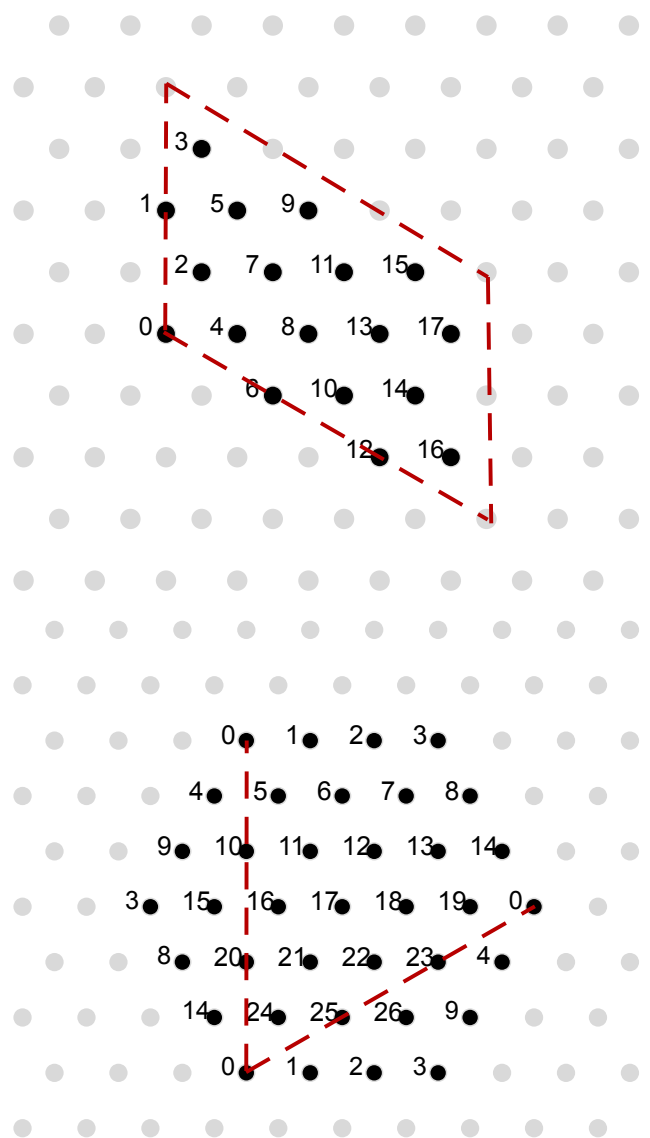


FIG. A.3. $N = 18$ and $N = 27$ clusters with periodic boundary conditions, utilized for exact diagonalization calculations.

a representative cluster that has dimensions 17×6 lattice constants - this accommodates a robust charge order throughout the entire cylinder (except the edges). On systems that had an even number of lattice constants in the horizontal direction (not shown), the 2×2 charge orders propagate from the left and right edges, creating domains that result in the appearance of a liquid-like region at the domain wall (the center of the cylinder).

Fig. A.2c shows results for the $t - V_1 - V_2 - V_3$ model. In this case, the formation of stripes, unlike the case of the torus, does not extend throughout the width of the cylinder (at least for long cylinders). Instead the system tends to form only short stripes. This is likely due to the energetic reduction that can be achieved from enhanced quantum fluctuations associated with shorter stripes. Additionally, the parameters of the $t - V_1 - V_2 - V_3$ place the

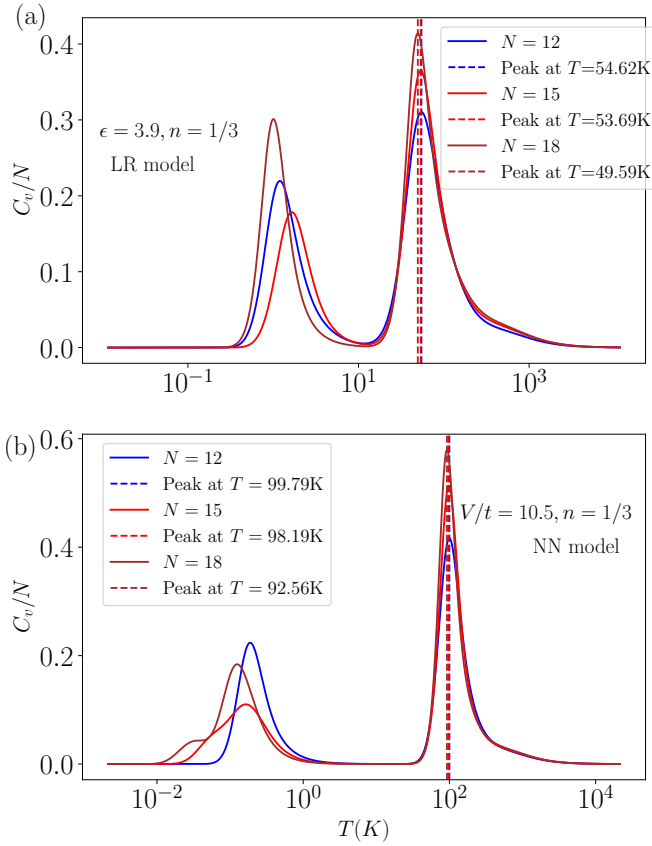


FIG. A.4. Specific heat C_v/N computed with full diagonalization (a) for the long-range model and (b) nearest-neighbor model for three system sizes $N = 12, 15, 18$. The parameters used are indicated on the figures.

system near a classical phase boundary (note, that the classical model has many exact degeneracies) suggesting sensitivity to boundary effects. Further investigation is required to probe the nature of the bulk ground state in the thermodynamic limit.

Appendix C: Cluster geometries used for exact diagonalization

In the main text we performed ED calculations to compute both zero and finite temperature properties. The $N = 12$ and $N = 15$ clusters utilized were considered in previous work [19]. In Fig. A.3 we show the $N = 18$ and $N = 27$ clusters with periodic boundary conditions that were utilized for ED calculations in this work.

Appendix D: Finite size effects on features of the specific heat

In the main text we presented results for the specific heat of classical models ($t = 0, U \rightarrow \infty$) for a wide range of system sizes. Despite obvious limitations from finite-

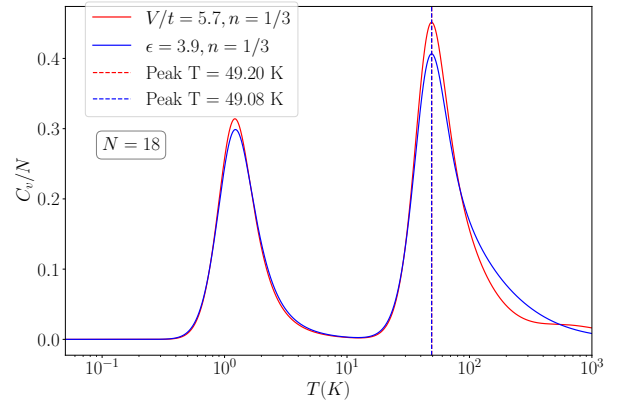


FIG. A.5. Specific heat C_v/N of the long-range model with $\epsilon = 3.9$ plotted together with that of the nearest neighbor model with $V_{1,\text{eff}}/t = 5.7$ for the case of $d/a = 10$.

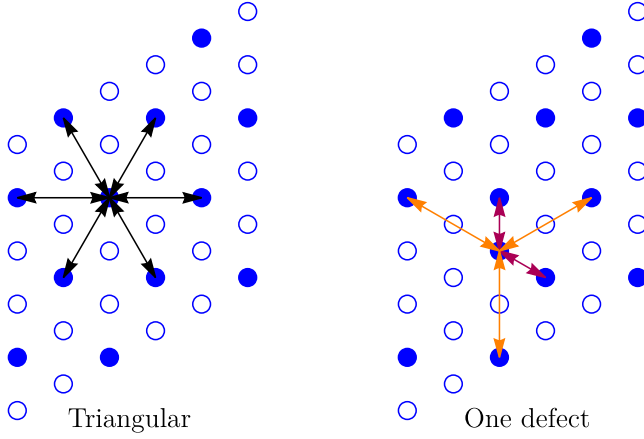
size effects, meaningful trends could be extracted even from the smallest system sizes that were studied. For example, the location of the charge peak, corresponding to the melting of the triangular GWC, moves to lower temperature on increasing the system size (the $N = 27$ and 36×36 were within about 10% of one another).

We show that similar conclusions hold at the quantum level by plotting the specific heat (C_v/N) for the LR model (Fig. A.4a) and the NN model (Fig. A.4b) for $N = 12, 15$ and 18 site systems. Parameter sets used are indicated on the figure. Each cluster accommodates the $\sqrt{3} \times \sqrt{3}$ triangular GWC ground state. The high temperature feature sharpens with increasing system size, narrowing in extent achieving a higher maximum of specific heat, consistent with a peak that signals the melting of the Wigner crystal. The location of the peak moves to lower temperature on increasing system size. The low temperature feature (bump) is expected to be a crossover associated with the destruction of short range magnetic order. The movement of these low temperature features is likely more involved and requires a better understanding of the effective magnetic Hamiltonian that governs the physics at low energy scales.

Appendix E: Determination of $V_{1,\text{eff}}$ from the long-range model

In the main text we showed that certain properties of the LR model can be mimicked by an effective NN model (see Fig. 4). This was particularly important when trying to understand why the GWC melting temperature did not change significantly with d/a .

This extraction of $V_{1,\text{eff}}$, the effective NN interaction strength, was done in two complementary ways. In the first method, purely classical in nature, a single charge in a $\sqrt{3} \times \sqrt{3}$ triangular GWC was moved to a neighboring vacant site to create a “defect” in the crystal. Both the GWC and representative defect configuration are shown



$$\Delta E = (2V_1 + 3V_3 + 6V_4 \dots) - (6V_2 + 6V_5 \dots) = 2V_{1,\text{eff}}$$

FIG. A.6. The left panel shows the $\sqrt{3} \times \sqrt{3}$ GWC and the underlying triangular lattice. The right panel shows a configuration where a single charge is moved to the nearest neighbor site, creating a “defect” in the GWC. In both cases the some (not all) of the non-zero contributions to the Coulomb energy are highlighted, the expression corresponds to the energy difference between the two configurations, which is thus the energy of a single defect.

in Fig. A.6. For a given d/a , the energy difference between the defect configuration and the defect-free crystal was computed and defined to be $2V_{1,\text{eff}}$ - this is the energy cost of a defect in the effective NN model. Fig. A.6 graphically depicts the Coulomb energy contributions associated with both configurations. The corresponding expression suggests that their subtraction leads to effective cancellations of the long range tail. It is this cancellation that leads to an energy difference that is (almost) independent of d/a .

In the second method, the quantum mechanical specific heat was computed for the LR model for a given d/a . Then keeping t unchanged, the quantum specific heat was computed for the NN model for a grid of values of $V_{1,\text{eff}}$, chosen in steps of $0.1t$. The optimal $V_{1,\text{eff}}$ was chosen to be the one which minimized the error between the two specific heat curves. An example of one such optimization has been presented in Fig. A.5.

Appendix F: Magnetic interactions of GWC at $n = 1/3$

The question of magnetism of GWCs in the moire TMDs remains an active area of research. In this Appendix we present some estimates of the GWC melting (crossover) temperature for $n = 1/3$ as a function of V/t in the NN model. Strictly speaking, there is no true long-range magnetic order in two dimensions at finite temper-

ature, so there is no sharp peak in the specific heat at low temperature, and we associate T_m with the location

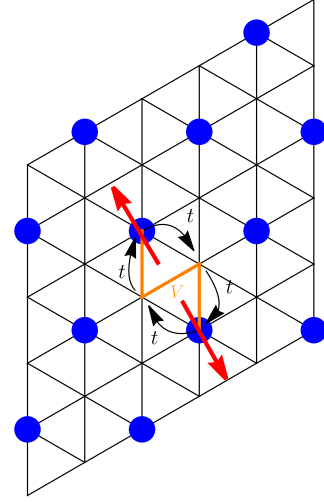


FIG. A.7. Schematic for the exchange process of two particles with opposite spin involving four hops, that gives rise to the effective magnetic interaction. Three orange solid line show the NN interaction V which occurs during the hops.

of the local maximum.

For V/t large (and assuming U/t is even larger), where the charge order corresponds to the $\sqrt{3} \times \sqrt{3}$ crystal, the magnetic exchange between two particles with opposite spins is generated (to lowest order) by an exchange process that involves four hops (two hops for each particle) on the underlying triangular lattice, shown in Fig. A.7. This gives rise to a magnetic exchange scale J that is expected to scale as t^4/V^3 . We see evidence of this scale indirectly in T_m which scales as the same power (see Fig. A.8). We plot physical estimates for T_m in Kelvin, incorporating the overall scale factor coming from t , which clarifies what temperatures should be probed in future experiments.

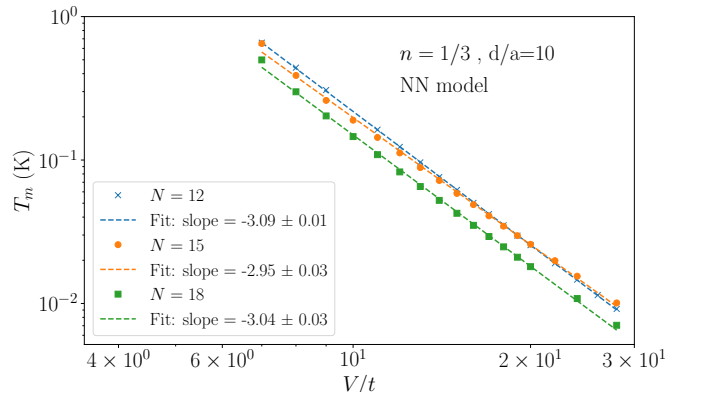


FIG. A.8. Magnetic crossover scale T_m as a function of NN interaction V/t . The overall factor of t is incorporated in T_m to clarify what temperatures should be probed in experiments